

Dual-gradient metal layer for practicalizing high-energy lithium batteries

Received: 26 February 2025

Accepted: 14 July 2025

Published online: 25 July 2025



Mengyu Tian^{1,2}, Ronghan Qiao², Guanjun Cen², Li Tian¹, Liubin Ben¹,
Hailong Yu², Michael De Volder³, Chenglong Zhao⁴, Qidi Wang⁵✉ &
Xuejie Huang^{1,2}✉

Pairing high-energy nickel-rich cathodes with current collectors as anodes presents a compelling strategy to significantly boost the specific energy of rechargeable lithium-ion batteries, driving progress toward a transportation revolution. However, the limited active lithium inventory sourced by the cathodes tend to be rapidly consumed by irreversible Li plating/stripping and interfacial side reactions. To address these limitations, we propose a dual-gradient metal layer as an innovative solution to mitigate active Li loss by promoting uniform Li deposition and in situ formation of a stable solid electrolyte interphase. The operation of these batteries is investigated using a combination of electrochemical and chemical techniques to differentiate dead Li and interphase-bound Li inventory loss as well as material characterization methods to analyse the plated Li and interfacial composition and morphology. The developed dual gradient metal layer-based 600 mAh $\text{LiNi}_{0.9}\text{Co}_{0.05}\text{Mn}_{0.05}\text{O}_2 \parallel \text{Cu}$ pouch cells achieve an areal capacity of 7.25 mAh cm^{-2} and deliver an 80% capacity retention over 160 cycles. We show that the proposed approach is compatible with a range of different metal materials, offering a promising path toward next generation long-lasting, high-energy, initially active material-free anode based Li metal batteries.

Rechargeable lithium (Li)-ion batteries (LIBs) have become the dominant energy carriers for modern urban traffic ranging from e-scooters to electric vehicles, due to their high specific energy, good cycle life (1000 – 10,000 cycles) and cost-efficiency^{1,2}. The emergence of low-altitude electric aircrafts, such as electric vertical takeoff and landing (EVTOL), along with the uptake of drones and humanoid robots, are creating an urgent demand for light-weight ultra-high specific energy battery technologies^{3,4}. Traditional LIBs, based on “rocking-chair” chemistry, face inherent specific energy limitations, and a radical approach to overcome this challenge is to omit the anode host material and instead plate and strip Li on an anode current collector. In

particular, if these initially active material-free anode based Li metal batteries (IFLMBs) are paired with high specific energy nickel-rich layered cathodes ($\text{LiNi}_x\text{Co}_y\text{Mn}_{1-x-y}\text{O}_2$, $x \geq 0.90$), they offer the potential for a step-change in specific energy ($\sim 500 \text{ Wh kg}^{-1}$ / $\sim 2000 \text{ Wh L}^{-1}$) while at the same time reducing the anode’s material and manufacturing cost (Fig. 1a and Table S1). However, the combination of a “zero excess Li” design (i.e. no Li pre-coated on the anode) and energy storage by plating and stripping introduces significant challenges, primarily stemming from a rapid depletion of the Li inventory delivered by the cathode. This active Li loss is driven by the formation of isolated Li (dead-Li) and continuous reconstruction of the solid electrolyte

¹Songshan Lake Materials Laboratory, Dongguan 523808 Guangdong, China. ²Beijing National Laboratory for Condensed Matter Physics Institute of Physics, Chinese Academy of Sciences 3rd South Street, Zhongguancun, Beijing 100190, China. ³Department of Engineering University of Cambridge, Cambridge CB3 0FS, UK. ⁴Shenzhen Key Lab of Energy Materials for Carbon Neutrality Shenzhen Institute of Advanced Technology, Chinese Academy of Sciences Shenzhen, Shenzhen 518055, China. ⁵Department of Mechanical and Energy Engineering, Southern University of Science and Technology, Shenzhen 518055, China. ✉ e-mail: wangqd@sustech.edu.cn; xjhuang@iphy.ac.cn

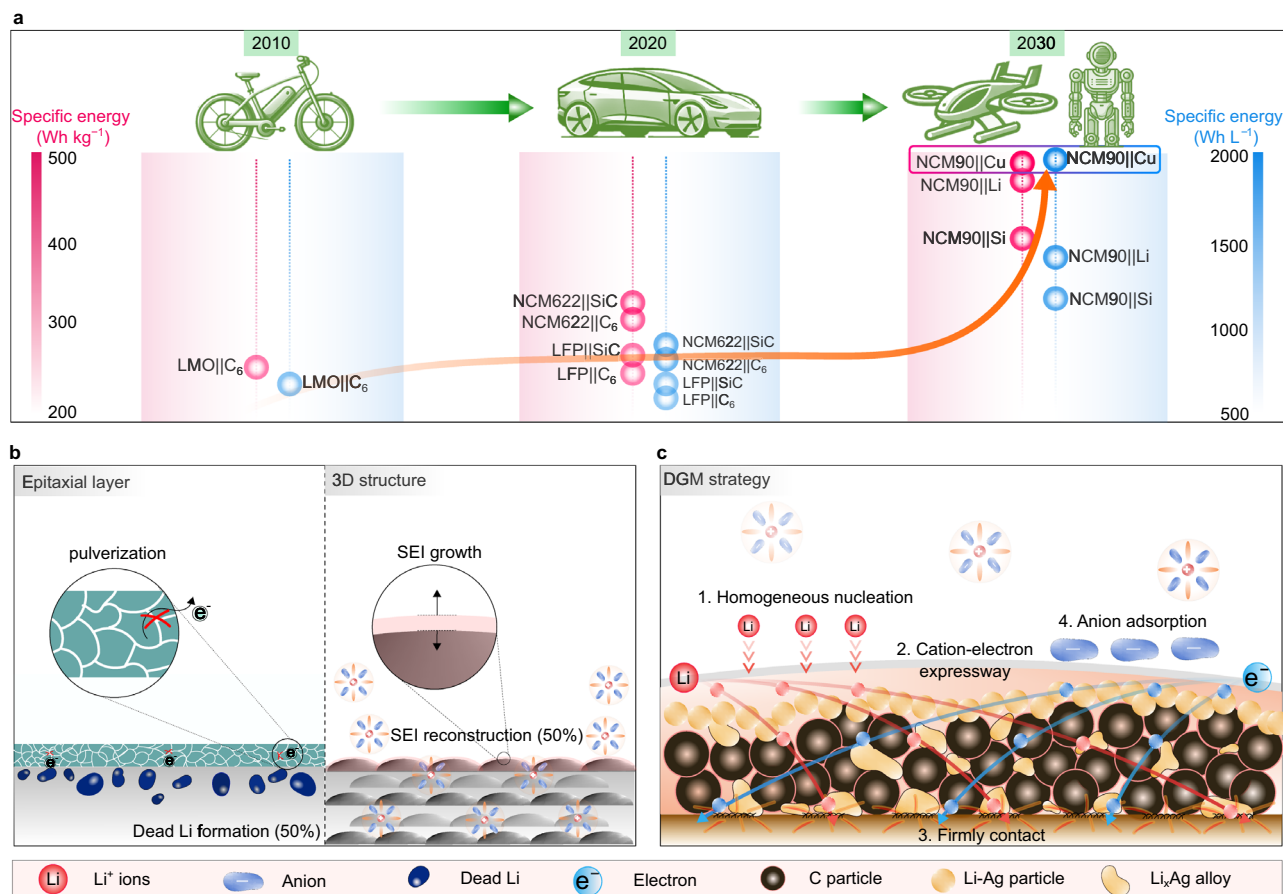


Fig. 1 | Conceptual illustration of the dual-gradient metal (DGM) layer.

a Historical development of achievable volumetric specific energy (Wh L^{-1}) and gravimetric specific energy (Wh kg^{-1}) across the three generations power batteries

(detailed parameters available in Tables S2–S9). **b** Illustration of irreversible active Li loss in zero-excess lithium metal batteries (IFLMBs) during prolonged cycling. **c** Schematic representation of the DGM layer structure.

interphase (SEI-Li) (Fig. 1b), and typically results in life-times of less than 100 cycles^{5,6}.

To address the challenges associated with active Li loss, various strategies have been explored. For instance, highly fluorinated electrolyte, salts and additives have gained recognition for their ability to construct inorganic species with superior mechanical stability and electrochemical insulation properties^{7–9}. While impressive advances have been made in this field, current strategies have only resulted in lifetimes exceeding 100 cycles when combined with low specific energy cathode, limited voltage ranges, and/or limited areal capacities which all limit the specific energy and therefore undermine the goal of achieving $\sim 500 \text{ Wh kg}^{-1}$ and $\sim 2000 \text{ Wh L}^{-1}$.

Here we address all the above challenges by focusing on the design of the current collectors and high specific energy cathode designs, which results the IFLMBs achieving over 500 Wh kg^{-1} with a good capacity retention of 80% after 160 cycles. A challenge previously reported for Cu current collectors is the high plating overpotential and uneven Li nucleation, which stems from the crystal structure mismatch between Li and Cu (Cu: 1.28 \AA vs. Li: 1.52 \AA), leading to uneven Li plating¹⁰. Strategies to homogenize plating rely on epitaxial metal layer Li deposition and three-dimensional (3D) current collectors to promote compact and uniform Li plating^{10–13} (Fig. 1b). In the first approach, metal-seed layers with a low nucleation overpotential such as Ag, Au, In, Mg, and Sn are coated on the current collector, which tends to alloy with Li prior to Li plating and reduces the interfacial energy between the substrate and Li metal^{8,14}. However, these metal layers undergo significant volume expansion and uneven stress during lithiation, resulting in accelerated pulverization and physical degradation¹⁵.

Additionally, the thermodynamically driven Li concentration gradient promotes metal agglomeration, leading to the further failure of metal layers during subsequent Li dissolution cycles¹⁶. In the second approach, 3D current collectors with high specific surface areas are used to lower the local current density and accommodate the plated Li in the pores to reduce electrode swelling during cycling. However, if these 3D scaffolds are too thick, they negate the enhancement in volumetric density offered by IFLMBs designs, and if their surface area is too high, they promote further SEI growth and degradation.

In this work, we judiciously balance the above approaches by proposing a dual gradient metal (DGM) anode design, which consist of a three layers structure with Cu foil as current collector on which a thin ($\sim 3 \mu\text{m}$) 3D composite metal (Me: metals of Al, Zn, Sn, Ag and so on)-carbon (C) is coated that is covered by a dense lithiophilic Me layer (Fig. 1c). The DGM layer is designed to simultaneously mitigate active Li loss by addressing two key challenges: the continuous accumulation of dead Li (i.e., Li metal regions which are electronically disconnected from the current collector) and the undesirable side reactions during extended cycling. This strategy operates through the following mechanisms: 1) The lithiophilic outer Me layer offers abundant nucleation sites, reducing nucleation overpotential. Its undulating structure alleviates high local current densities and uneven stress distribution, ensuring homogeneous initial Li deposition and maintaining structural integrity. 2) The inner porous MeC layer, with its mixed ionic-electronic conductivity, accommodates the volume expansion of Li metal during the plating/stripping process while enabling rapid charge-transfer reactions. 3) C particles provide mechanical support to the Li-Me-C nanocomposite layer due to their

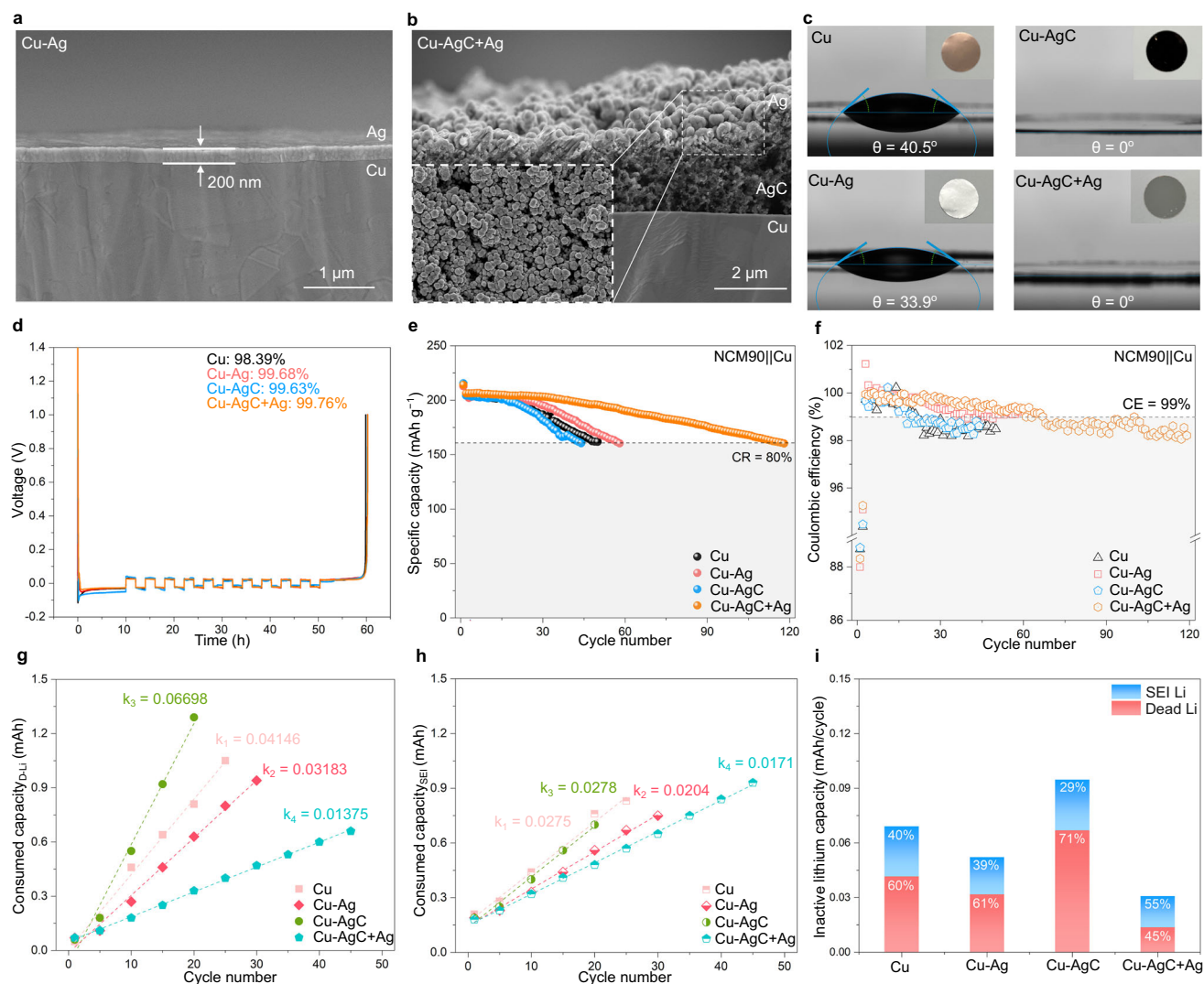


Fig. 2 | Electrochemical performance of the DGM layer. a, b Cross-sectional SEM images of Cu-Ag and Cu-AgC+Ag electrodes. **c** Contact angle measurements and optical image of Cu, Cu-Ag, Cu-AgC and Cu-AgC+Ag electrodes. **d** Voltage-time profiles and initial voltage-capacity curves of various Li||Cu cells at a current density of 0.5 mA cm^{-2} . **e, f** Cycle performance and coulombic efficiency of the

NCM90 || Cu full cells at a low current rate of $0.1/0.1 \text{ C}$ for conditioning (1 cycle) and standard current rate of $0.2/0.33 \text{ C}$ for cycling between 4.4 to 3.0 V ($1 \text{ C} = 240 \text{ mA g}^{-1}$). **g–i** Evolution of consumed dead-Li and SEI-Li, calculated using TGC and electrochemical methods during cycling. All electrochemical testing were conducted at $25 \pm 1^\circ \text{C}$.

high modulus, preventing the aggregation of Me and ensuring that the Li-Me alloy remains firmly adhered to the Cu current collector. 4) The MeC clusters exhibit strong interactions with FSI^- anions, facilitating the formation of a stable, anion-derived SEI layer. Furthermore, systematic electrochemical and morphological studies confirm the effectiveness of the DGM layer in enabling dendrite-free Li deposition and stabilizing the SEI layer. Remarkably, the prototype NCM90 || Cu pouch cell achieves an impressive specific energy of 503 Wh kg^{-1} , 1931 Wh L^{-1} (cell level) and high capacity retention of 80% after 160 cycles.

Results and discussion

Electrode design and failure analysis

In this study, we found a surprising dependence of the cycling performance on the current collector morphology. We demonstrate this first using an Ag lithiophilic coating, where we either coat a continuous Ag solid film on Cu current collector, or on top of a porous AgC layer, which results in a granular Ag top layer with an average grain size of $50\text{--}100 \text{ nm}$ (see the experimental section and Supplementary Note 1). Figure 2 illustrates the key characteristics of AgC, Ag and AgC+Ag

layers as well as their impact for electrochemical performance. As discussed above the Ag layer in Cu-Ag and Cu-AgC+Ag electrodes exhibit distinct structures (Figs. 2a, b and S1), despite having similar thicknesses of approximately 200 nm . For Cu-AgC+Ag electrode, the inner porous AgC layer, consisting of Ag and C particles, provides a fluctuating substrate for the subsequent deposition of the outer Ag layer with high electron conductivity ($6.3 \times 10^{-7} \text{ S m}^{-1}$)¹⁴. While adding a $3 \mu\text{m}$ AgC layer on Cu prior to Ag coating is subtle, it has vast implications in the cycling stability as discussed further, which we believe are due to: (i) porosity and undulation of the Ag layer releasing stress induced by the volume changes during alloying of Ag to Li_xAg . (ii) The porous AgC with high specific surface area (Fig. S2 and Supplementary Note 1) creates a capillary pull for electrolyte infiltration¹⁷, decreasing the electrolyte contact angle (Fig. 2c), and promotes rapid charge-transfer reactivity (Fig. S3). (iii) The composite porous electrode creates an environment in which Li^+ can be transported rapidly and electrochemically be reduced to metallic Li, creating a flexible and expandable scaffold for Li deposition.

To verify the effectiveness of DGM layer in optimizing Li nucleation behavior, Li||Cu cells were assembled following the standard

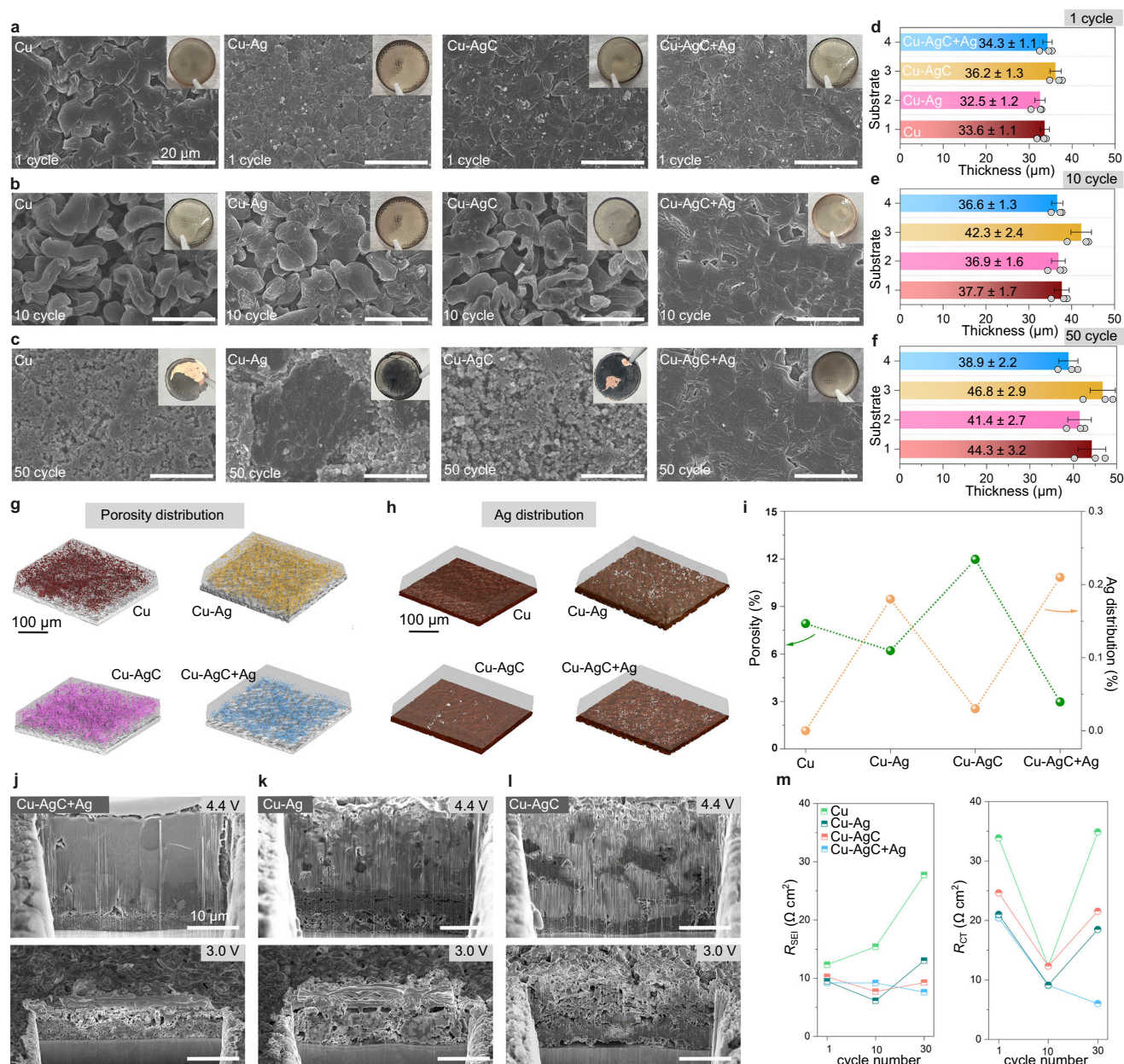


Fig. 3 | Morphological and structural evolution of deposited Li metal. a–c Top-view SEM images and **d–f** thickness variations of the deposited Li metal on Cu, Cu-Ag, Cu-AgC and Cu-AgC+Ag electrodes between cycle 1st and cycle 50th with an area capacity of 6.5 mAh cm^{-2} from NCM90 || Cu based cells, and data are presented as mean values \pm standard deviation (Data points are three randomly selected thickness values). **g, h** 3D reconstructed morphology using X-ray computed tomography (CT), showing porosity/cracks and Ag distribution at fully charged state (4.4 V) from NCM90 || Cu based cells with an area capacity of 6.5 mAh cm^{-2} in cycle 10th. **i** Quantification of porosity and Ag content percentage of deposited Li

metal across different electrodes. **j–l** Cross-sectional SEM images obtained via FIB milling, illustrating deposited Li metal at 4.4 V (fully charged) and 3.0 V (discharged) after 30th cycled in NCM90 || Cu cells with an area capacity of 6.5 mAh cm^{-2} . **m** Fitted Nyquist plots of NCM90 || Cu cells at the discharged state of 3.0 V, recorded from the 1st to 30th cycles. All electrochemical testing were conducted at $25 \pm 1^\circ\text{C}$, NCM90 || Cu full cells were cycled at a low current rate of 0.1/0.1 C for conditioning (1 cycle) and standard current rate of 0.2/0.33 C for cycling between 4.4 to 3.0 V ($1\text{C} = 240 \text{ mA g}^{-1}$) before disassembling.

procedure¹⁸. The Li || Cu-AgC+Ag cells show the highest average coulombic efficiency [98.39% (Cu) vs. 99.68% (Cu-Ag) vs. 99.63% (Cu-AgC) vs. 99.76% (Cu-AgC+Ag), Fig. 2d], lowest nucleation overpotential [86.3 (Cu) vs. 18.2 (Cu-Ag) vs. 45.2 (Cu-AgC) vs. 12.3 mV (Cu-AgC+Ag), Figure S4] and polarization potential [56.4 (Cu) vs. 51.2 (Cu-Ag) vs. 57.5 (Cu-AgC) vs. 48.9 mV (Cu-AgC+Ag), Figure S5]. During the initial Li plating stage, the epitaxial Ag layer eliminate nucleation barrier and provide ordered lithophilic nucleation sites for Li embryo growth (Figure S6 and Supplementary Note 2). Meanwhile, the underlying AgC layer, which contains abundant Ag nanoparticles, further promotes the

downward deposition of metallic Li and accommodates volume expansion during repeated plating/stripping cycles (cf. Figure 3).

The influence of the DGM layer on cycle life is evaluated in combination with a high-nickel layered cathode, specifically $\text{LiNi}_{0.9}\text{Co}_{0.05}\text{Mn}_{0.05}\text{O}_2$ (NCM90), using a high-areal capacity (6.5 mAh cm^{-2}) and large voltage window (3.0–4.4 V) to maximise the cell specific energy. Remarkably, NCM90 || Cu-AgC+Ag full cell retains 80% of their capacity after 120 cycles (Fig. 2e), which is comparable to other IFMBs reported in the literature with various modification strategies (Table S10). However, NCM90 || Cu+Ag cell only has a slight

improvement compared with the reference NCM90||Cu cell, and the NCM90||Cu-AgC cell exhibits even lower capacity retention. Notably, all NCM90||Cu based cells have a similar degradation pattern, characterized by an initial stage of almost retained capacity [e.g., 20 cycles (Cu) vs. 60 cycles (DGM)], followed by an inflection point and a rapid linear decline, which corresponds with a sudden drop in CE to below 99% (Fig. 2f). These comparable electrochemical behaviors may be attributed to the depletion of latent active Li on the anode side. Approximately 10% active Li which cannot reinsert into the anode after the first delithiation process, stays on the anode side, serving as a reservoir of active lithium to compensate for lithium loss until the reservoir is exhausted¹⁹ (Fig. S7 and Supplementary Note 3). The point of depletion of this Li reservoir coincides well with the inflection point of specific capacity and CE.

For NCM90||Cu cells, active Li loss on anode side primarily governs the battery life, given superior stability of NCM90 cathode (Fig. S8). By combining electrochemical tests with titration gas chromatography, the evolution of inactive Li on the anode side, primarily consisting of dead-Li and SEI-Li, can be precisely monitored after specific cycles. This approach allows for a comprehensive evaluation of the factors contributing to capacity degradation^{18,20}. Figures S9 and S10 display reversible Li, active Li reservoir, dead-Li and SEI-Li capacity after cycling, in which active Li reservoir from DGM-based cell drains the slowest, e.g., 25 cycles (Cu) vs. 30 cycles (Ag layer) vs. 20 cycles (AgC layer) vs. 45 cycles (DGM), and detailed data are provided in Tables S11 and S12. Notably, the growth of dead-Li and SEI-Li follows a linear increase before the active Li reservoir runs out, which indicates that the build-up of inactive Li did not affect its subsequent reformulation behavior (Fig. 2g, h). As shown in Fig. S11 and Supplementary Note 4, the interlayer derived from residual active Li reservoir, rather than Cu substrates, dominates Li nucleation and deposition in next adjacent cycle, as illustrated by Powder X-ray diffraction (PXRD) patterns at different states of charge (SOC)²¹, which is responsible for the linear accumulation pattern of dead-Li and SEI-Li.

Figure 2i exhibits significant difference in SEI-Li related capacity loss across four substrates with the accumulation rate of SEI-Li proportional to that of dead-Li. For instance, Cu-AgC+Ag electrode effectively promotes uniform and dense Li metal deposition and preserved the integrity of SEI during cycling, decreasing the consumption of SEI-Li (Figs. 3 and 4)^{22–24}. Furthermore, the differences in SEI thickness and uniformity affect the local uniformity and flux of Li⁺ diffusion in SEI layer, which in turn influences the deposition morphology and structure of Li metal. Consequently, the DGM-based NCM90||Cu cell shows lowest dead-Li and SEI-Li loss, with values of 13.8 and 17.1 uAh per cycle, respectively, significantly extending the cycle life of anode-free cells. In the following section, a detailed explanation of the mechanism by which the DGM layer regulates the Li electrochemical deposition/dissolution process and optimizes the nanostructure and composition of the SEI layer will be provided.

Morphological properties coupling with different substrates

Figure 3a–c show the morphology evolution of deposited Li in representative NCM||Cu based cells after the 1st, 10th and 50th cycles. After the first charge to 4.4 V, the deposited Li on the DGM layer, Ag layer and AgC layer all exhibit a denser structure compared to the reference Cu-based cell. Further, the DGM-based anodes still maintain a uniform and planar Li deposition after 50th cycles with silvery metallic shine; while other counterparts underwent a morphological transition from wire-like and dendritic Li structure (10 cycle) to pulverized mossy Li (50 cycle), and metallic Li have blackened and fallen away from the current collector. And the growth of these whisker Li is more prone to losing structural connection, leading to an increased amount of dead-Li. Moreover, the DGM-based Li deposition demonstrates minimal thickness variation even after 50 cycles, with measurements of 34.2 μm (1st cycle), 35.1 μm

(10th cycles), and 37.5 μm (50th cycles) (Figs. 3d–f and S12). These values closely align with the theoretical thickness of deposited Li on pristine Cu substrate (31.5 μm), confirming the DGM strategy's effectiveness in maintaining uniform and dense Li plating/stripping throughout prolonged cycling¹⁸.

To examine the 3D structural features of the plated Li without damaging its internal microstructure during cell disassembly, X-ray computed tomography (CT) was employed to analyze the deposited Li after 10th cycles (Fig. S13). CT imaging leverages the differential attenuation of X-ray intensity as it passes through materials with varying densities, allowing the spatial distribution of pores, Li bulk, and Ag particles to be distinguished based on luminance differences²⁵. Figure 3g exhibits the 3D reconstructed image for pores distribution, revealing that the Cu-AgC+Ag electrode has the lowest porosity of 3.06%. This finding highlights the ability of the DGM layer to suppress the formation of pores during the Li plating process. By doing so, the DGM layer might reduce the surface area of Li being exposed to the electrolyte, thereby mitigating side reactions²⁶.

Additionally, Ag could fully dissolve into Li and form Li_xAg alloy in any proportion¹⁴, which appears to be a key factor in optimizing the Li growth pattern, promoting uniform Li deposition, and enhancing rapid Li transport. However, during the dissolution process, homo-dispersed Ag particles tend to agglomerate, following the Ostwald ripening mechanism, and gradually mix with electrochemically inactive materials, leading to the failure of the epitaxial metal layer. As shown in Fig. 3h, i, both the Cu-Ag and Cu-AgC+Ag electrodes exhibit a similar reunited Ag volume percentage of approximately 0.2 vol%, while the Cu-AgC electrode shows a negligible value due to its lower initial Ag content. Importantly, these Ag nuclei were small and evenly dispersed in the Cu-AgC+Ag electrode; while the Ag nuclei in the Cu-Ag electrode were significantly larger and enriched in specific areas. This demonstrates that the DGM layer effectively suppresses the undesired agglomeration of Ag particles, maintaining their dispersion and promoting stable and uniform Li deposition¹⁶, as further discussed below.

To further explore the significant differences in deposited Li morphology and deposition behavior, focused ion beam–scanning electron microscopy (FIB–SEM) sections were employed after 30 cycles, as illustrated in Figs. 3j–l and S14. The Cu-AgC+Ag electrode exhibits smooth and plane surface with fractional contrast difference after charging to 4.4 V. And the lithiated AgC nanocomposite layer is tightly anchored to the current collector, indicating stable integration of the DGM layer (Fig. 3j). Upon discharging to 3.0 V, the outer Ag layer still maintains initial granular morphology, demonstrating its resilience to structural changes. In contrast, partial active Li dissolve from the inner AgC layer and reserve space for subsequent Li deposition, serving as respiratory effect to eliminate inchoate volume change, and the well-preserved Li-Ag-C composite layer support sufficient electron and ionic path and reduces the interfacial impedance with the Cu current collector, as demonstrated in Electrochemical impedance spectroscopy (EIS) measurement²⁷ (Fig. 3m).

In sharp contrast, the lower part of deposited Cu-Ag electrode shows loose and uneven structure with higher porosity and aggregated Ag block (Figs. 3k and S15), which also dominates the nonuniform properties of the epitaxial growth of upper Li deposition. And the initial compact and uniform Ag film was not recovered after Li dissolution, replacing by the hybrid layer of pores, dead-Li (considering that active Li reservoir was almost consumed for NCM90||Cu-Ag cell after 30 cycles, Fig. 2) and Ag block with sluggish electron and Li⁺ transportation kinetics. As the Ag film gradually expands during lithiation, its internal strain/stress accumulates due to the different Li concentration difference¹⁵, which causes the fragment and formation of Ag block. And these Ag block may be further surrounded with dead-Li and SEI layer, leading to its final failure. Moreover, the Ag agglomeration induced failure behavior is related to the discharge current (*i*),

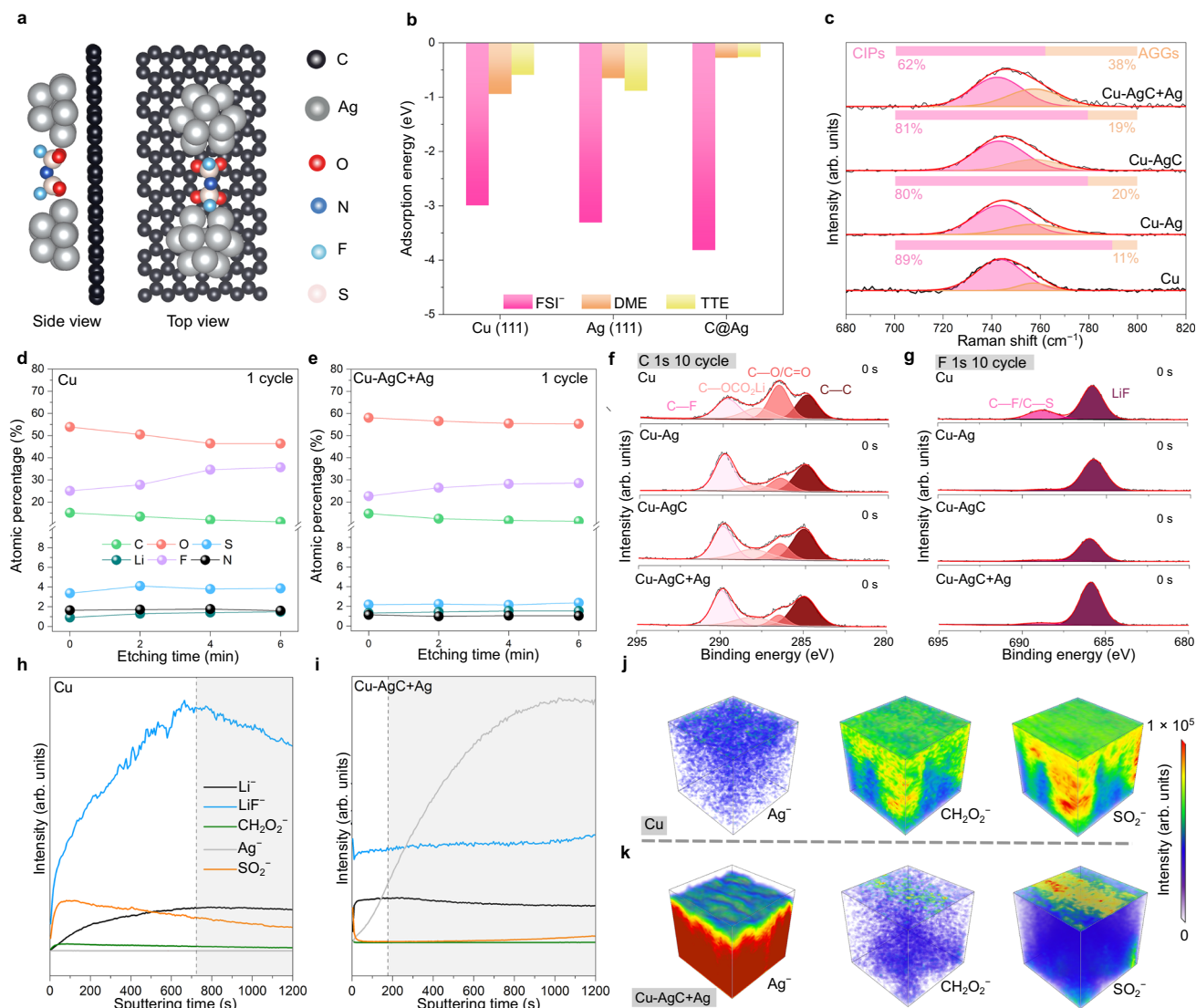


Fig. 4 | Chemical composition and spatial structure of DGM-mediated interphase layer. a, b FSI⁻ adsorption models and corresponding adsorption energies of FSI⁻, DME and TTE molecule adsorption energy on different current collector (CC). **c** Raman spectra of localized high-concentration electrolytes (LHCE) electrolyte on different CC. **d**, **e** Atomic percentages of the element detected by the XPS measurements, see more details in Figs. S18 and S19. **f**, **g** XPS profiles of C 1s

and F 1s spectra on different CC after 10th cycles at 3.0 V. **h**, **i** TOF-SIMS traces of the Cu and Cu-AgC+Ag electrodes after 10th cycles at 3.0 V. **j**, **k** Selected secondary-ion fragments of Cu and Cu-AgC+Ag electrode after 10th cycles detected by TOF-SIMS. The samples used for XPS and TOF-SIMS measurements were disassembled from NCM90 || Cu based cells with an area capacity of 6.5 mAh cm⁻² at discharged state (3.0 V).

which could be described in the following Eq. 1¹⁶:

$$i = -FD_{Li}c_{Li}\nabla\ln a_{Li} \quad (1)$$

where F is Faraday's constant, D_{Li} is Li diffusivity in the alloy, c_{Li} is the Li concentration and $\nabla\ln a_{Li}$ is the gradient of Li activity in alloy layer, and $\nabla\ln a_{Li}$ determines the Ostwald ripening behavior of Ag as a direct driving force. For DGM strategy, on the one hand, the porous AgC layer magnify specific surface area and reduce local current density during delithiation process, which suppresses the initial driving force for initial Ag nucleation; on the other hand, the mechanically stable C particles with high modulus of 200 GPa support the lithiated AgC layer as skeleton and cut off the path for the bottom Ag to gather²⁸ (Fig. S14).

As shown in Fig. 3l (Cu-AgC electrode), portions of the AgC layer (i.e., the dark sections) are pulled into the Li bulk due to stress migration during the charging process. Additionally, significant areas of the AgC layer detach from the Cu current collector after the delithiation process. For Cu-AgC electrode, the uneven volume expansion

caused by random nucleation of Li embryo results in uneven stress distribution (Fig. S6). This leads to the layer-by-layer detachment and pulverization of the AgC clusters, which in turn triggers a cascade of side reactions and an avalanche-like accumulation of dead Li. These effects degrade the electrochemical performance of the Cu-AgC electrode, making it inferior to the reference Cu substrate.

EIS measurements after 30th cycles illustrate that the DGM-based cell has a lowest charge-transfer resistance, e.g., 6.2 (DGM) vs. 18.6 (Cu-Ag) vs. 21.2 (Cu-AgC) vs. 34.6 Ω cm² (Cu), suggesting that the mixed electron-ion hybrid dual channel (lithiated DGM layer) closely attached to current collector enhance electron transport kinetic (Figs. 3m and S16), which is definitely conducive to the reversible transformation of active Li⁺ and metallic Li. And the resistance decreases from cycle 1 to cycle 10 might be related to the activation process. Moreover, the R_{SEI} of NCM90 || Cu is significantly higher than the other three cells, revealing the sluggish transportation process of Li⁺ through its SEI layer, which usually connected with spatial structure, chemical composition and thickness characters of SEI layer (Fig. 4).

The less resistive SEI on DGM-based cell, in turn, enable good Li transport, which leads to less dead Li formation as discussed in Fig. 2.

Design of inner Helmholtz plane and SEI nanostructure

Density functional theory (DFT) simulations and Raman spectroscopy were applied to investigate Li ions solvation structure near substrate surface and the inner Helmholtz plane (IHP) composition (Figs. 4a and S17), which govern the initial SEI components and their characters. As shown in Fig. 4b, compared to Cu and Ag substrates, the AgC cluster exhibits the highest adsorption energy for FSI^- and lowest adsorption energy for DME and TTE solvents, e.g., -3.8134 (FSI^- , AgC) vs. -0.2738 (DME, AgC) vs. -0.2587 eV (TTE, AgC); and -3.8134 (FSI^- , AgC) vs. -3.3075 (FSI^- , Ag) vs. -2.9902 eV (FSI^- , Cu). These results indicate that the DGM layer enhances anion adsorption on the IHP, facilitated by its extensive Ag@C interactions^{29,30}. Moreover, the combination of Ag and AgC in the DGM layer may generates synergistic effect, exerting an additional adsorption of FSI^- , as studied by Raman spectra below. Figure 4c further exhibits the Raman spectra of electrolyte covered on substrates, focusing on regions closest to the substrate. All electrodes show the absence of a free FSI^- peak ($\sim 717\text{ cm}^{-1}$), and the Cu-AgC+Ag electrode demonstrates the highest proportion of aggregate clusters (AGGs, 38%) and contact ion pairs (CIPs, 62%). This indicates the intensified interaction between Li^+ and FSI^- is driven by the strong anion adsorption effect of Ag@C cluster, which, in turn, promotes the formation of a stable SEI layer dominated by inorganic species³¹.

To elucidate the chemical principles underlying the formation of a stable SEI layer with minimal SEI-Li consumption on the surface of the DGM layer-based electrode, the chemical compositions and their spatial distributions were meticulously analyzed using XPS and TOF-SIMS³². Figures 4d, e, and Figs. S18 and S19 exhibit the atomic percentage variations over sputtering time. The Cu-AgC+Ag electrode shows a similar elemental distribution to the Cu-AgC and Cu-Ag electrodes attributed to the modified adsorption features of substrate. In contrast, the pristine Cu has a significantly higher S content and undulant F content, e.g., S (4.2%, 6 min) and F (25.1%, 0 min) vs. F (36.7%, 6 min), which reveals the over-decomposition of electrolyte on the surface of pristine current collector (Fig. S18 and Supplementary Note 5). After 10-activation cycles, the O content is the lowest for the DGM-based electrode, particularly after sputtering, e.g., 57.5% (Cu) vs. 58.6% (Cu-Ag) vs. 58.7% (Cu-AgC) vs. 48.3% (Cu-AgC+Ag) after sputtering for 360 s, suggesting that the decomposition of organic DME and TTE solvents are suppressed with DGM layer³³, thereby promoting the formation of a stable and inorganic species-dominated SEI layer (Supplementary Note 6).

In the high-resolution C 1s spectra, the peaks assigned to C–O/ C = O (286.4 eV) and R–OCO₂Li (287.8 eV) dominate the C-containing species for Cu electrode (Fig. 4f and Table S13). Additionally, the F 1s spectra of the Cu electrode reveal a higher content of unstable C–F/S–F (688.2 eV), indicating that the SEI layer on the unmodified Cu electrode contains a significant proportion of loose organic components³⁴. This porous SEI layer fails to effectively isolate the contact between electrolyte and metallic Li, resulting in continuous interfacial side reactions and higher SEI-Li consumption (i.e., 0.0275 mAh per cycle). In contrast, the chemical composition of the SEI layer from Cu-Ag, Cu-AgC and Cu-AgC+Ag exhibit almost identical compositions (Figs. S20–S23), characterized by a high content of LiF-dominated inorganic species and a lower proportion of sulfurized and oxidized organic species. The inherent adsorption nature of these modified substrate attracts more FSI^- anions in IHP, forming an inorganic-dominant bilayer SEI after first cycle³⁵. However, their SEI-Li consumption behavior differs significantly. In subsequent cycles, SEI-Li accumulation is closely tied to the Li deposition behavior. The uniform and compact Li plating/stripping enabled by the DGM layer minimizes SEI layer cracking, reduces exposure of fresh metallic Li, and limits

continuous electrolyte decomposition. As a result, the capacity loss associated with SEI-Li is significantly reduced, emphasizing the critical role of the DGM layer in enhancing electrode stability.

To quantitatively monitor the variation of the selected chemical species in the SEI layer, the TOF-SIMS measurements of the cycled Cu electrode were conducted³⁶, focusing on specific organic species (e.g., CH_2O_2^- and SO_2^-) and inorganic species (LiF) identified earlier through XPS analysis (Fig. 4h, i, S24 and Supplementary Note 7). The signal related to the residual bulk Li phase (i.e., Li^+) reaches a peak value for the Cu-AgC+Ag sample after sputtered by Cs^+ ions for less than 200 s while the Cu electrode presents a gradually intensified Li^+ signal until sputtering for 600 s, indicating the ultrathin nature of DGM-based SEI layer. The CH_2O_2^- , SO_2^- and LiF related species are derived from the decomposition of electrolyte (i.e., DME, TTE and LiFSI) and could be used as a judgment for measuring interfacial stability³⁷. The CH_2O_2^- , SO_2^- and LiF contents are significantly lower for Cu-AgC+Ag electrode than that for Cu electrode, and these species mainly enrich in the surface region for the former one. Notably, even though the relative proportion of these species are almost the same for all substrates as shown in XPS (cf. Fig. S19), the actual absolute content from the reference Cu electrode is obviously higher, which reveals extra electrolyte decomposition. Figures 4j–k and S25–S28 illustrate the spatial distribution of selected secondary-ion fragments. For the Cu-AgC+Ag SEI layer, decomposition products are uniformly distributed in the outer region. In contrast, for the reference Cu electrode, these decomposition species penetrate deeper into the SEI layer, mixing with bulk Li. Furthermore, the Cu-AgC+Ag electrode exhibits a high concentration and uniform distribution of Ag^- , which further contributes to the stability and compactness of the SEI layer.

Combined with the overall results, the enhanced interfacial stability in DGM electrodes can be illustrated as follows: the AgC cluster in the DGM layer adsorbs massive FSI^- anions within the IHP layer, which governs the initial interfacial evolution process. This results in the formation of an ultrathin, inorganic species-dominated SEI layer characterized by exceptional chemical, electrochemical, and mechanical stability. Such a robust SEI layer effectively suppresses electron leakage, inhibits Li dendrite growth, and minimizes electrolyte decomposition. Moreover, the DGM layer's electron conductivity, mechanical compliance and increased surface area facilitate uniform and dense Li plating/stripping, avoiding the formation of pores and inactive Li. This further preserves the SEI layer's integrity, protecting it from mechanical fractures and repeated regeneration cycles. However, the loose and fragile SEI formed on the Cu electrode induces a serious adverse chain reactions involving its continuous thickening, leading to the rapid active Li consumption and cycle performance degradation. This comparison highlights the critical role of the DGM layer in stabilizing the electrode interface and improving long-term battery performance.

Practicalizing DGM layer for high-energy anode-free battery

Compared to prototype coin cells, pouch cells are widely used to evaluate the applicability of new materials for practical application in EVTOLs integration due to their key parameters—such as electrode area, areal loading, and electrolyte/capacity ratio—that closely resemble those of commercial cells³⁸. To fully access the large-scale feasibility of DGM layer, we fabricated industrial-level DGM electrode and assemble multilayer pouch cell with 600 mAh according to a standard assembly protocol developed in Songshan Lake Materials Laboratory (Table S14 and Fig. S29). Remarkably, the DGM-based pouch cells achieve a high specific energy of 503 Wh kg^{-1} and 1931 Wh L^{-1} (cell level), significantly surpassing the limits of conventional rocking-chair chemistry-based batteries. As shown in Figs. 5a, b and S30, the DGM-based anode free NCM90 || Cu pouch cells, with a high areal capacity of 7.25 mAh cm^{-2} demonstrate great cycling performance, retaining over 80% after 160 cycles at 0.2/0.33 C under a constant stack pressure of

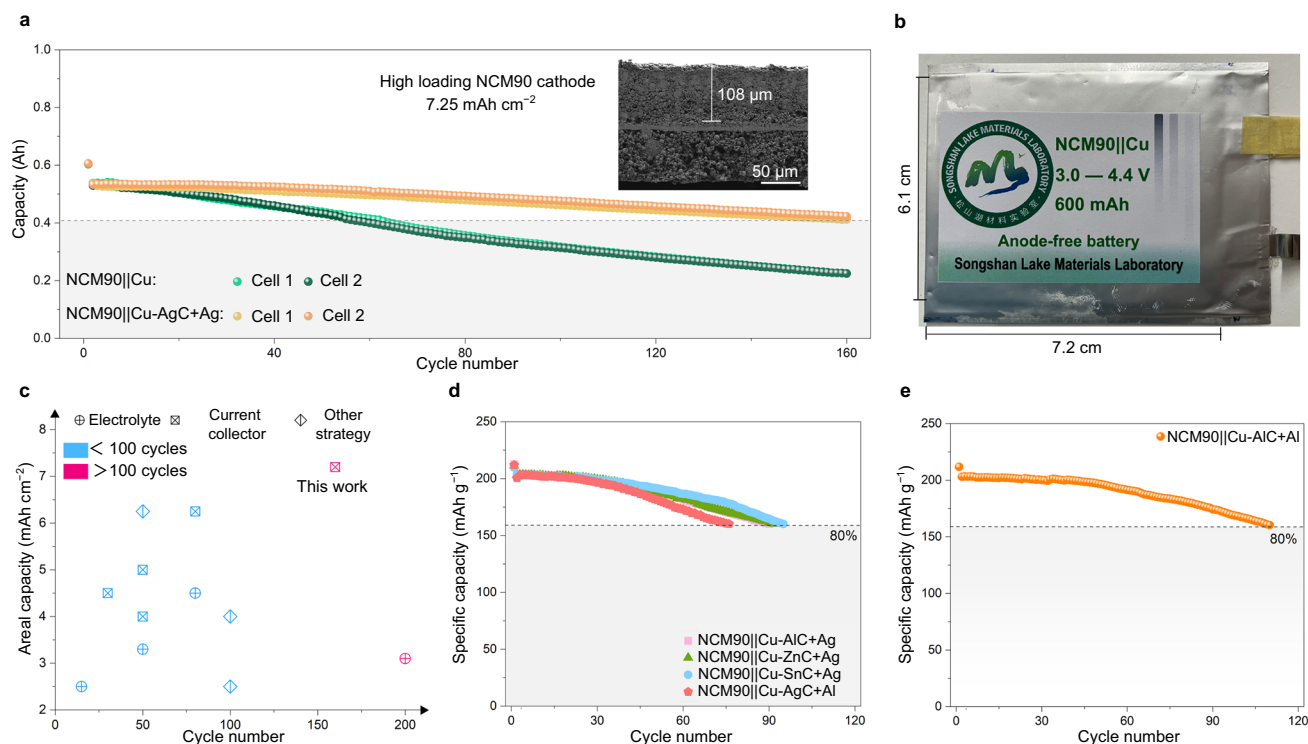


Fig. 5 | Electrochemical performance of DGM-based pouch cells. a, b Cycle performance and optical image of 600 mAh DGM-based NCM90 || Cu pouch cell operating between 3.0 and 4.4 V and the corresponding reference pouch cells ($1\text{ C} = 240\text{ mA g}^{-1}$), and the cross-sectional SEM image of high-loading NCM90

cathode (32 mg cm^{-2}). **c** Comparison of area capacity and cycled life in various NCM || Cu cells using different modification methods for pouch cells. **d, e** Cycle performance of additional DGM-based NCM90 || Cu cells. All electrochemical testing were conducted at $25 \pm 1^\circ\text{C}$ ($1\text{ C} = 240\text{ mA g}^{-1}$).

1.0 MPa (Fig. S31). This performance surpasses the state-of-the-art results reported in the literature for other modification strategies (Fig. 5c and Table S15). In contrast, the reference NCM || Cu cells achieve an 80% capacity retention over 50 cycles. The obvious improvement in cycling stability has been consistently validated by duplicate experiments (i.e., cell 1 and cell 2), clearly highlighting the pivotal role of the DGM layer in extending the cycle life of high-energy IFLMBs.

To comprehensively assess the scalability of DGM layer, we expand of the DGM concept to other materials, for instance, displacing the Ag nanoparticles from inner layer with Al, Zn and Sn nanoparticles, and replacing the outer Ag layer with Al layer (Figs. S31 and S32). These alternative DGM-based electrode achieve cycle life of up to 100 (Figs. 5d and S33), underscoring the potential of the DGM layer to increase the cycling stability of IFLMBs. In particular, Al based NCM90 || AlC+Al cells provide an interesting balance between cost efficiency and an 80% capacity retention for over 100 cycles (Figs. 5e and S34). These results suggest that DGM layer, as a universal methodology, effectively extends the lifespan of IFLMBs via eliminating accumulation of dead-Li and SEI-Li, while alleviating concerns for the reliance of DGM strategies on specified metals (Fig. S35 and Supplementary Note 8).

In summary, we introduce a dual-gradient layer strategy that regulates uniform Li plating/stripping behavior through alloying reaction with lithiophilic metals. The DGM layer consists of a carbon base layer mixed with Ag nanoparticles and a top Ag providing sites for Li nucleation and a stable interface with the Cu current collector. Additionally, the strong adsorption of FSI⁻ anions from the interaction with the AgC cluster facilitates the formation of a LiF-rich inorganic SEI layer, protecting against parasitic side reactions. The incorporation of this DGM layer significantly enhances the cycle life and specific energy of Ah-level pouch cells. Moreover, this approach is adaptable to other low-cost metals such as Al, Zn, and Sn. The DGM layer strategy

provides a revolutionary advancement for practical IFLMBs, driving high energy battery technology, and supporting the widespread deployment of EVTOLs and humanoid robots.

Methods

Materials

$\text{LiNi}_{0.9}\text{Co}_{0.05}\text{Mn}_{0.05}\text{O}_2$ (NCM90) powder was prepared by calcining a mixture of $\text{Ni}_{0.9}\text{Co}_{0.05}\text{Mn}_{0.05}(\text{OH})_2$ precursor, $\text{LiOH}\cdot\text{H}_2\text{O}$, and a small amount of Nb_2O_5 additive (0.5 wt%) at 750°C for 15 h in a flowing oxygen atmosphere using a tube furnace; battery-grade electrolyte and electrode materials (>99.95% purity) were sourced from commercial suppliers: metallic Li sheet (14 and 15 mm, thickness = 0.6 mm, China energy lithium), *N*-methyl pyrrolidone (NMP, Acros Organics), lithium bis(fluorosulfonyl)amide (LiFSI, Aladdin), Ag nanoparticles ($D_{50} = 50\text{ nm}$, Aladdin), Ag nanoparticles ($D_{50} = 50\text{ nm}$, Aladdin), Sn nanoparticles ($D_{50} = 50\text{ nm}$, Xiangtian nano), Al nanoparticles ($D_{50} = 50\text{ nm}$, Xiangtian nano), Zn nanoparticles ($D_{50} = 50\text{ nm}$, Xiangtian nano). The electrolyte solvents of 1,2-dimethoxyethane (DME, 99%) and 1,1,2,2-Tetrafluoroethyl 2,2,3,3-tetrafluoropropyl ether (TTE, 98%) were provided by Aladdin.

Preparation of DGM layer

The metal nanoparticles (e.g., Ag, Sn, Al and Zn) were pre-mixed with Super-P (SP) in a weight ratio of 1:3 and stirred with the mixing solution of 10 wt% poly(vinylidene difluoride (PVDF, HF Keijing, $M_w = 4 \times 10^5$) in NMP for 30 min. The solid content of this slurry is 30 wt%. After fully stirring, the slurry was then coated on the Cu foil with a 25 μm blade (Kemai) and dried at 80°C (air) for 20 min and 120°C (vacuum) for 6 h. The Ag and Al epitaxial layers was further plating by magnetron sputtering (SP600, Hengyue vacuum) with a working rate of 1 \AA s^{-1} for ca. 1000 s at 10^{-6} Torr. The thickness of AgC composite layer was 3 to 5 μm and the thickness of metal epitaxial layer was ca. 200 nm.

General characterizations

X-ray diffraction analysis (PXRD) of the electrodes was performed on a Bruker D8 Advance instrument employing Cu K α radiation ($\lambda = 1.5406 \text{ \AA}$). Data collection spanned 10° to 80° (2θ) at a step width of 0.0198° . Field emission scanning electron microscopy (FE-SEM, ZEISS Gemini 300) at an accelerating voltage of 5 kV was utilized to examine the deposited Li surface morphology, cross-sectional thickness variation, and elemental distribution via EDS mapping. The focused ion beam (FIB, Thermofisher Helios SUX) with Ga $^+$ ion beam (30 kV, 9.1 nA) was used to mill the cycled Cu electrode for further analysis, and these samples were prepared in glove box with a homemade vacuum chamber. The Raman spectra of electrolyte on different substrates were detected by a confocal Raman microscope (Horiba, LabRam HR Evolution) with a 532 nm laser.

Atomic force microscopy (AFM, Oxford Instruments Cypher S) operating in contact mode quantified the average roughness and current distribution of the pristine substrates. Samples' chemical compositions (e.g., post-reaction solid phases, electrode surfaces) were analyzed using X-ray photoelectron spectroscopy (XPS, Thermo Fisher ESCALAB XI+) with a nonmonochromatic Al K α source ($h\nu = 1486.6 \text{ eV}$). High-resolution spectra were acquired under low-power conditions (100 W, 20 eV pass energy, 0.05 eV step size). To compensate for charging effects, all spectra were referenced to the C 1s peak at 284.8 eV. Prior to transfer into the XPS chamber via a homemade vacuum system, samples underwent gentle DME rinsing followed by thorough vacuum drying.

Time-of-flight secondary ion mass spectrometry (TOF-SIMS, ION-TOF M6) provided additional characterization of the electrode-electrolyte interphase. Sputtering was performed with a 1 keV Cs $^+$ ion beam. All target secondary ions were acquired at a mass resolution $>30,000$. Consistent with XPS sample preparation, electrodes were rinsed with DME, dried thoroughly under vacuum, and transferred into the TOF-SIMS chamber via a homemade vacuum system.

Electrode preparation

The cathode slurry was formulated by combining NCM90 cathode-active material (94 wt%), PVDF binder (3 wt%), and SP conductive carbon (3 wt%, Alfa-Aesar) in NMP. This slurry was coated onto a 9- μm thick aluminum foil and dried at 80°C for 6 h to form the cathode electrode sheet. The resulting NCM90 electrodes exhibited an active material loading density of 28 mg cm^{-2} . Subsequently, the electrode sheets were punched into discs (15 mm diameter for anode, 14 mm for cathode) and subjected to further drying at 120°C for 6 h prior to assembly into coin cells. (The Cu foil thickness is $4.5 \mu\text{m}$).

X-ray microscope and reconstruction

For micro-CT samples, the cycled anode electrode was disassembled from NCM90||Cu cells after 10 cycles at fully charged state (i.e., 4.4 V) and washed with DME for three times. Then the electrode was cut into $3 \times 3 \text{ mm}^2$ and encapsulated with transparent sealing tape in glove box. All samples were analyzed by micro-CT (Xradia Versa610) for 2 h and reconstructed by dragonfly. Deep learning embedded in the Dragonfly software was used for further analysis of micro-CT images, and the U-net network was used as the deep learning architecture³⁹. To train the deep learning model, images containing different morphologies were selected to identify Li-metal bulk, pores/cracks and Li $_x$ Ag alloy. OrsDiceLoss and Adadelata were employed as the loss function and algorithm, respectively.

Computational details

All spin-polarized total energy calculations were carried out using the Vienna Ab Initio Simulation Package (VASP) with the projector augmented wave (PAW) method based on density functional theory (DFT)⁴⁰. The generalized gradient approximation (GGA) was

employed to describe the exchange-correlation potential, using the Perdew-Burke-Ernzerhof (PBE) parametrization. Additionally, the van der Waals interactions were accounted for using Grimme's DFT-D3 correction^{41,42}. The first model employed Ag (111) with lattice parameters $a = 10.0 \text{ \AA}$, $b = 17.3 \text{ \AA}$, and $c = 22.1 \text{ \AA}$, and a $2 \times 1 \times 1$ Gamma k-point mesh for Brillouin zone integration. For simulating interactions with the AgC layer, a single graphene sheet was used as a substrate to host the Ag clusters, with lattice parameters $a = 25.6 \text{ \AA}$, $b = 12.3 \text{ \AA}$, and $c = 20.4 \text{ \AA}$. For Cu (111), the lattice parameters were $a = 8.6 \text{ \AA}$, $b = 17.9 \text{ \AA}$, and $c = 21.3 \text{ \AA}$. All structures were fully relaxed until the force on each atom was less than 0.02 eV/\AA , with an energy convergence threshold of 10^{-5} eV . The calculation parameters and configurations are provided in Supplementary Data 1–4.

Electrochemical measurements

CR2032 coin-type full cells were assembled in an argon-filled glovebox (Braun MB-Unilab Pro SP) using anode/cathode disks, a Celgard 2400 separator (thickness = $25 \mu\text{m}$, diameter = 16.2 mm , porosity = 40% and average pore size = $0.117 \mu\text{m} \times 0.042 \mu\text{m}$), and 1.5 M LiFSI-DME/TTE (2:8, v/v) localized highly concentrated electrolyte (LHCE), cycled at $25 \pm 1^\circ\text{C}$ using a LAND (Wuhan LAND) tester. Coulombic efficiency (CE) was measured in Li||Cu half-cells by first plating 5 mAh cm^{-2} of Li onto the Cu substrate, followed by cycling at a fixed capacity of 1 mAh cm^{-2} (constant current density: 0.5 mA cm^{-2}) until stripping to 1.0 V vs. Li/Li $^+$, with CE calculated as the ratio of stripped-to-plated capacity. NCM90||Cu full cells were cycled between 3.0–4.4 V using a protocol of 0.1 C charge/0.1 C discharge for 1 formation cycle, followed by 0.1 C charge/0.33 C discharge for subsequent cycles, while NCM90||Cu-AgC+Ag pouch cells were tested under identical cycling conditions with a constant stacking pressure of 1 MPa. The Li||Cu cells use stainless steel based disks with 1 spacer (0.6 mm) and 1 spring, while the NCM||Cu cells use aluminum-coated disks with 3 spacers (0.6 mm) and 1 spring. All coin batteries were injected with 120 μl electrolyte.

Electrochemical impedance spectroscopy (EIS) measurements (potentiostatic mode) were conducted in the frequency range of 1.0 MHz–0.01 Hz with a 5 mV amplitude at $25 \pm 1^\circ\text{C}$, and the number of data points were 66. NCM90||Cu cells were measured at 1, 10, and 30 cycles after full discharge to 3.0 V. The open-circuit voltage before the testing was 3.0 V, and the fluctuation was less than 3 mV within 0.5 h.

Titration gas chromatography

The cycled NCM90||Cu cells after different cycles were disassembled in the argon-filled glovebox, and the glovebox pressure was then lowered to 1 atm before titration experiment. The cycled Cu electrode and separator were sealed in a 30 mL flask with parafilm (M parafilm, PM 996) and tape, and 1 ml deionized water was injected by a syringe with needle to fully react with electrochemically inactive lithium. After shaking for three minutes and no bubbles generating, 0.5 ml mixed gas was collected by self-locking syringe (Hamilton, 81256) and injected into a Gas Chromatograph (ThermoFisher, Trace 1300). Based on the ratio of H $_2$ peak ($t \approx 1.375 \text{ min}$) area to the known standard gas (C $_{\text{H}_2}$ = 2 mol%) H $_2$ peak area, the content of inactive lithium metal is further calculated as shown below:

$$x = \frac{\frac{S_1}{S_2} \times 2\% V_1 \times M_{\text{Li}} \times C_{\text{Li}}}{V_2}$$

where x is the capacity of inactive lithium metal, S_1 is H $_2$ peak area of tested gas, S_2 is H $_2$ peak area of standard gas, V_1 is the volume of flask (i.e., 30 ml), V_2 is the molar volume of gas (i.e., 24.5 L, 25°C , $1.01 \times 10^5 \text{ Pa}$), M_{Li} is the molar mass of lithium (i.e., 6.941 g mol^{-1}) and C_{Li} is the theoretical capacity of lithium (i.e., 3860 mAh g^{-1}).

Data availability

The authors declare that all data supporting the findings of this study are available within the paper, its Supplementary Information and Source Data file. Source data are provided with this paper.

References

- Armand, M. & Tarascon, J. M. Building better batteries. *Nature* **451**, 652–657 (2008).
- Tian, M. et al. Designer lithium reservoirs for ultralong life lithium batteries for grid storage. *Adv. Mater.* **36**, 2400707 (2024).
- Viswanathan, V. et al. The challenges and opportunities of battery-powered flight. *Nature* **601**, 519–525 (2022).
- Sripad, S. & Viswanathan, V. The promise of energy-efficient battery-powered urban aircraft. *Proc. Natl. Acad. Sci.* **118**, e2111164118 (2021).
- Shi, J. et al. In situ p-block protective layer plating in carbonate-based electrolytes enables stable cell cycling in anode-free lithium batteries. *Nat. Mater.* **23**, 1686–1694 (2024).
- Huang, C.J. et al. Decoupling the origins of irreversible coulombic efficiency in anode-free lithium metal batteries. *Nat. Commun.* **12**, 1452 (2021).
- Zhang, Q.-K. et al. Homogeneous and mechanically stable solid-electrolyte interphase enabled by trioxane-modulated electrolytes for lithium metal batteries. *Nat. Energy* **8**, 725–735 (2023).
- Li, T. et al. Deciphering lithium deposition behavior in elemental alloy anodes for lithium metal batteries. *Nano Lett.* **24**, 15234–15241 (2024).
- Louli, A. J. et al. Diagnosing and correcting anode-free cell failure via electrolyte and morphological analysis. *Nat. Energy* **5**, 693–702 (2020).
- Yan, K. et al. Selective deposition and stable encapsulation of lithium through heterogeneous seeded growth. *Nat. Energy* **1**, 16010 (2016).
- Lin, L. et al. Epitaxial induced plating current-collector lasting life-span of anode-free lithium metal battery. *Adv. Energy Mater.* **11**, 2003709 (2021).
- Sohn, Y. et al. Dual-seed strategy for high-performance anode-less all-solid-state batteries. *Adv. Mater.* **36**, 2407443 (2024).
- Cao, J. et al. Li_2ZnCu_3 Modified Cu current collector to regulate Li deposition. *Angew. Chem., Int. Ed.* **64**, e202413065 (2024).
- Zhang, S. et al. Phase diagram determined lithium plating/stripping behaviors on lithiophilic substrates. *ACS Energy Lett.* **6**, 4118–4126 (2021).
- Wang, Y. et al. Control of Two Solid Electrolyte Interphases at the Negative Electrode of an Anode-Free All Solid-State Battery based on Argyrodite Electrolyte. *Adv. Mater.* **37**, 2410948 (2025).
- Thenuwara, A. C. et al. High-rate and stable LLZO-based lithium-metal batteries enabled via a tin interlayer. *ACS Energy Lett.* **9**, 2401–2409 (2024).
- Cui, H., Song, Y., Ren, D., Wang, L. & He, X. Electrocapillary boosting electrode wetting for lithium-ion batteries. *Joule* **8**, 29–44 (2024).
- Lin, X., Shen, Y., Yu, Y. & Huang, Y. In situ NMR verification for stacking pressure-induced lithium deposition and dead lithium in anode-free lithium metal batteries. *Adv. Energy Mater.* **14**, 2303918 (2024).
- Louli, A. J. et al. Optimizing cycling conditions for anode-free lithium metal cells. *J. Electrochem. Soc.* **168**, 020515 (2021).
- Gervillie-Mouravieff, C., Ah, L., Liu, A., Huang, C.-J. & Meng, Y. S. Deciphering the impact of the active lithium reservoir in anode-free pouch cells. *Acs Energy Lett.* **9**, 1693–1700 (2024).
- Spencer-Jolly, D. et al. Structural changes in the silver-carbon composite anode interlayer of solid-state batteries. *Joule* **7**, 503–514 (2023).
- Deng, W. et al. Quantification of reversible and irreversible lithium in practical lithium-metal batteries. *Nat. Energy* **7**, 1031–1041 (2022).
- Chen, H. et al. Synthesis of monocrystalline lithium for high-critical-current-density solid-state batteries. *Nature Synth* **4**, 552–561 (2025).
- Zhang, E. et al. Monofluorinated acetal electrolyte for high-performance lithium metal batteries. *Proc. Natl. Acad. Sci.* **122**, e2418623122 (2025).
- Choi, P., Parimalam, B., Li, Y. & Litster, S. Operando ultra-high-resolution X-ray microscopy of lithium anodes with separator interactions. *J. Power Sources* **581**, 233468 (2023).
- Li, G.X. et al. Enhancing lithium-metal battery longevity through minimized coordinating diluent. *Nat. Energy* **9**, 817–827 (2024).
- Lim, K., Popovic, J. & Maier, J. Ion transport and growth behavior of solid electrolyte interphases on Li and Na with liquid electrolytes based on impedance analysis. *J. Mater. Chem. A* **11**, 5725–5733 (2023).
- Lee, Y.G. et al. High-energy long-cycling all-solid-state lithium metal batteries enabled by silver-carbon composite anodes. *Nat. Energy* **5**, 299–308 (2020).
- Ma, S. et al. Modulating the inner helmholtz plane towards stable solid electrolyte interphase by anion- π interactions for high-performance anode-free lithium metal batteries. *Angew. Chem., Int. Ed.* **137**, e202412955 (2024).
- Zhang, D. et al. A novel cathode interphase formation methodology by preferential adsorption of a borate-based electrolyte additive. *Natl. Sci. Rev.* **11**, nwae219 (2024).
- Li, Y. et al. Construction of a robust solid electrolyte interphase on Ge anode to achieve a superior long-term cycle life of lithium-ion battery. *J. Alloy. Compd.* **954**, 170200 (2023).
- Tian, M. et al. Domino reactions enabling sulfur-mediated gradient interphases for high-energy lithium batteries. *J. Am. Chem. Soc.* **145**, 21600–21611 (2023).
- Olana, B. N. et al. Understanding the formation chemistry of native solid electrolyte interphase over lithium anode and its implications using a LiTFSI/TME-TTE electrolyte and polysulfide additive. *J. Mater. Chem. A* **12**, 3659–3670 (2024).
- Gebresilassie Eshetu, G. et al. Ultrahigh performance all solid-state lithium sulfur batteries: salt anion's chemistry-induced anomalous synergistic effect. *J. Am. Chem. Soc.* **140**, 9921–9933 (2018).
- Kwon, H. et al. Borate-pyran lean electrolyte-based Li-metal batteries with minimal Li corrosion. *Nat. Energy* **9**, 57–69 (2024).
- Sheng, L. et al. Suppressing electrolyte-lithium metal reactivity via Li^+ -desolvation in uniform nano-porous separator. *Nat. Commun.* **13**, 172 (2022).
- Wu, Z. et al. Deciphering and modulating energetics of solvation structure enables aggressive high-voltage chemistry of Li metal batteries. *Chem* **9**, 650–664 (2023).
- Lin, L. et al. Li-Rich $\text{Li}_2[\text{Ni}_{0.8}\text{Co}_{0.1}\text{Mn}_{0.1}]\text{O}_2$ for anode-free lithium metal batteries. *Angew. Chem., Int. Ed.* **60**, 8289–8296 (2021).
- Ju, P. et al. Designer particle morphology to eliminate local strain accumulation in high-nickel layered cathode materials. *ACS Energy Lett.* **8**, 3800–3810 (2023).
- Hohenberg, P. & Kohn, W. Inhomogeneous electron gas. *Phys. Rev. B* **136**, B864 (1964).
- Monkhorst, H. J. & Pack, J. D. Special points for brillouin-zone intergrations. *Phys. Rev. B* **13**, 5188–5192 (1976).
- Perdew, J. P., Burke, K. & Ernzerhof, M. Generalized gradient approximation made simple. *Phys. Rev. Lett.* **78**, 1396–1396 (1997).

Acknowledgements

This work was supported by the National Key Research and Development Program of China (grant no. 2019YFA0705101), Guangdong Basic and Applied Basic Research Foundation (grant no. 2025A1515012904

and 2024A1515140081), China Postdoctoral Science Foundation (grant no. 2024M752304) and the National Natural Science Foundation of China (grant no. 22409141 and 22179144).

Author contributions

X.H. and M.T. conceived the original idea, Q.W. and C.Z. directed the work. M.T., R.Q. and G.C. carried out the experiments and measurements. L.T. helped to develop the TGC analysis. M.T. and C.Z. performed the DFT calculations. L.B., H.Y. and M.V. assisted with characterization and results discussion. M.T., X.H., Q.W. and C.Z. wrote the initial draft, and all authors contributed to the writing of the final manuscript.

Competing interests

The authors declare no competing interests.

Additional information

Supplementary information The online version contains supplementary material available at <https://doi.org/10.1038/s41467-025-62163-5>.

Correspondence and requests for materials should be addressed to Qidi Wang or Xuejie Huang.

Peer review information *Nature Communications* thanks Howard Tu, and the other, anonymous, reviewer(s) for their contribution to the peer review of this work. A peer review file is available.

Reprints and permissions information is available at <http://www.nature.com/reprints>

Publisher's note Springer Nature remains neutral with regard to jurisdictional claims in published maps and institutional affiliations.

Open Access This article is licensed under a Creative Commons Attribution-NonCommercial-NoDerivatives 4.0 International License, which permits any non-commercial use, sharing, distribution and reproduction in any medium or format, as long as you give appropriate credit to the original author(s) and the source, provide a link to the Creative Commons licence, and indicate if you modified the licensed material. You do not have permission under this licence to share adapted material derived from this article or parts of it. The images or other third party material in this article are included in the article's Creative Commons licence, unless indicated otherwise in a credit line to the material. If material is not included in the article's Creative Commons licence and your intended use is not permitted by statutory regulation or exceeds the permitted use, you will need to obtain permission directly from the copyright holder. To view a copy of this licence, visit <http://creativecommons.org/licenses/by-nc-nd/4.0/>.

© The Author(s) 2025